HHS Public Access

Author manuscript

Adv Funct Mater. Author manuscript; available in PMC 2021 October 22.

Published in final edited form as:

Adv Funct Mater. 2020 October 22; 30(43): . doi:10.1002/adfm.202004838.

Maximizing Chiral Perturbation on Thermally Activated Delayed Fluorescence Emitters and Elaboration of the First Top-Emission Circularly Polarized OLED

Lucas Frédéric,
Université Paris-Saclay, CEA, INRAE, Département Médicaments et Technologies pour la Santé (DMTS) SCBM, Gif-sur-Yvette F-91191, France

Alaric Desmarchelier,
Université Paris-Saclay, CEA, INRAE, Département Médicaments et Technologies pour la Santé (DMTS) SCBM, Gif-sur-Yvette F-91191, France

Romain Plais,
Université Paris-Saclay, CEA, INRAE, Département Médicaments et Technologies pour la Santé (DMTS) SCBM, Gif-sur-Yvette F-91191, France

Leonid Lavnevich,
Université Paris-Saclay, CEA, INRAE, Département Médicaments et Technologies pour la Santé (DMTS) SCBM, Gif-sur-Yvette F-91191, France

Gilles Muller,
Department of Chemistry, San Jose Staté University, One Washington Square, San José, CA 95192-0101, USA

Cassie Villafuerte,
Department of Chemistry, San Jose Staté University, One Washington Square, San José, CA 95192-0101, USA

Gilles Clavier,
Université Paris-Saclay, ENS Paris-Saclay, CNRS, PPSM, Cachan 94235, France

Etienne Quesnel,
Université Grenoble-Alpes, CEA, LETI, MINATEC Campus, 17 rue des Martyrs, Grenoble 38054, France

Benoit Racine,
Université Grenoble-Alpes, CEA, LETI, MINATEC Campus, 17 rue des Martyrs, Grenoble 38054, France

Sylvia Meunier-Della-Gatta,

gregory.pieters@cea.fr .

Supporting Information

Supporting Information is available from the Wiley Online Library or from the author.

Conflict of Interest

The authors declare no conflict of interest.

Université Grenoble-Alpes, CEA, LETI, MINATEC Campus, 17 rue des Martyrs, Grenoble 38054, France

Jean-Pierre Dognon,
Université Paris-Saclay, CEA, CNRS, NIMBE, Gif-sur-Yvette 91191, France

Pierre Thuéry,
Université Paris-Saclay, CEA, CNRS, NIMBE, Gif-sur-Yvette 91191, France

Jeanne Crassous,
Université de Rennes, CNRS, ISCR – UMR 6226, Rennes 35042, France

Ludovic Favereau,
Université de Rennes, CNRS, ISCR – UMR 6226, Rennes 35042, France

Grégory Pieters
Université Paris-Saclay, CEA, INRAE, Département Médicaments et Technologies pour la Santé (DMTS) SCBM, Gif-sur-Yvette F-91191, France

Abstract

Molecular designs merging circularly polarized luminescence (CPL) and thermally activated delayed fluorescence (CP-TADF) using the concept of chiral perturbation appeared recently as a cornerstone for the development of efficient CP-organic light emitting diodes (CP-OLED). Such devices could strongly increase the energy efficiency and performances of conventional OLED displays, in which 50% of the emitted light is often lost due to the use of antiglare filters. In this context, herein, ten couples of enantiomers derived from novel chiral emitter designs are reported, exhibiting CPL, TADF, and aggregation induced enhancement emission properties (AIEE). Representing the first structure properties relationship investigation for CP-TADF materials, this thorough experimental and theoretical work highlights crucial findings on the key structural and electronic parameters (isomerism, nature of the carbazole substituents) governing the synergy between CPL and TADF properties. To conclude this study, the first top emission CP-OLED is elaborated as a new approach of generating CP light in comparison with classical bottom-emission CP-OLED architecture. Indeed, the top-emission configuration represents the only relevant device architecture for future microdisplay applications. Thereby, in addition to offer molecular guidelines to combine efficiently TADF and CPL properties, this study opens new avenues toward practical applications for CP-OLEDs.

Keywords

aggregation induced emission; circularly polarized luminescence; OLED; thermally activated delayed fluorescence

1. Introduction

OLEDs appear as one of the most promising technologies for lighting devices or screen displays. Based on the use of organic compounds as emissive dopants embedded within a matrix to emit light after electrical excitation, various advantages can be put forward for display application compared to standard LCDs. Most common among them are a

higher contrast ratio given by OLEDs, a faster response time, a minimal thickness, to name but a few. However, the main issue encountered with the use of organic materials as emitters in OLEDs resides in the deexcitation pathways. In OLEDs, due to quantum mechanics, 25% of the electrical energy is converted into singlet state excitons and 75% into triplet state excitons. Thus, for prompt fluorescence (PF) emitters, up to 25% of the energy input can be theoretically converted into light through fluorescent decay, while the remaining 75% excitons, in the triplet state, will be lost through non-radiative deexcitation. Thus, most fluorophores are not implemented in OLED devices because they only emit PF. In order to harvest both singlet and triplet excitons and convert those into light, phosphorescent compounds can also be used, taking advantage of intersystem crossing (ISC). However, they are often sensitive, expensive, rare metal-based compounds, or display low quantum yield. In this context, the use of thermally activated delayed fluorescence (TADF) materials has emerged as one of the best alternatives to construct efficient OLED devices.[1] TADF occurs when the energy difference between singlet and triplet states of the molecule is small enough, so that a rISC (reverse intercrossing system) allows triplet states to be converted into singlet ones. This opens up the possibility to design OLEDs with a theoretical quantum efficiency of 100%. For this reason, various molecular designs have been developed to produce molecules exhibiting energetically close lowest singlet state (S_1) and lowest triplet state (T_1) while maintaining as high a quantum yield as possible.[2] Because the singlet-triplet energy gap (ΔE_{ST}) is proportional to the highest occupied-lowest unoccupied molecular orbital (HOMO-LUMO) integral overlap, the most widespread strategy to minimize this ΔE_{ST} consists in using a twisted donor-acceptor (D-A) system, where HOMO and LUMO are spatially separated.[3]

In parallel to this approach, the design of efficient circularly polarized luminescent (CPL) emitters emerged as an important gateway to improve efficiency while decreasing the power consumption of portable OLED displays.[4] As opposed to lighting devices, displays need antiglare filters to avoid reflection of external light sources off their emitting surface (sunlight or public lighting for instance). The most commonly used filters are built with a quarter-wave plate and a polarizer. Unfortunately, such an architecture reduces the intensity of non-polarized light emitted by a conventional OLED display by at least 50%. A solution to this significant energy loss could lie in mastering the design of efficient CP-OLEDs able to emit polarized light. This way, with a high degree of polarization, the light emitted by the display could pass through the antiglare filter layers without any attenuation. Therefore, merging CPL and TADF into a single fluorophore recently appeared as the new frontier in the design of next-generation emissive dopants for display applications.[5] Molecular designs enabling the efficient combination of those properties in an organic molecule remain scarce (see Figure 1) because of the challenge that lies in obtaining high quantum yield ($\mathbf{\Phi}$), low ΔE_{ST} (for TADF emission) and good chiroptical properties (g_{abs} for absorption and g_{lum} for emission, see Supporting Information, page 18) at the same time. Hirata and coworkers were the first to report a CP-TADF pair of enantiomers in 2015, relying on a strategy where an asymmetric center is sandwiched in a TADF active donor-acceptor (D-A) chromophore.[6] These enantiomers possessing moderate quantum yields and a long delayed fluorescence lifetime were not applied as emitters in an OLED device despite their promising chiroptical properties (notably, a dissymmetry factor $g_{lum} = 1.1 \times 10^{-3}$ measured in toluene solution).

Then, our group published a new molecular design in 2016 using the concept of chiral perturbation, by tethering an enantiopure BINOL unit to a TADF chromophore.[7] A prototype compound displaying good quantum yield in solution (53% in degassed toluene) and $g_{lum} = 1.3 \times 10^{-3}$ was applied as the emitter in an OLED exhibiting an external quantum efficiency (EQE) of 9.1% (see isomer **A**, Figure 1). The high racemization barrier of the chiral perturbing unit has allowed to maintain the optical purity of the compound during device fabrication by thermal evaporating method, demonstrating the potential of such molecules in the construction of efficient CP-OLEDs. Using this molecular design, several other research groups have synthesized chiral TADF emitters, demonstrated their aggregation induced enhancement (AIEE) properties, and used them to construct efficient bottom-emission CP-OLEDs.[8] With BINOL derivatives as the acceptor, Cheng and workers have constructed CP-TADF molecules exhibiting g_{lum} values of up to 1.6×10^{-3}.[9] Another innovative molecular design involving two TADF chromophores templated by a chiral 1,2-diaminocyclohexane unit was subsequently developed by Chen and coworkers.[10] Thereafter, other intrinsically chiral TADF chromophores were reported. Zhao and coworkers reported the synthesis of chiral [2.2]-paracyclophane TADF emitters which, in spite of their attractive photophysical and chiroptical properties, were not used as emitters for the construction of CP-OLED.[11] Zysman-Colman et al. have used a chiral carbazolophane donor unit (indolo[2.2]paracyclophane) to design CP-TADF molecules showing interesting chiroptical properties ($g_{lum} = 1.3 \times 10^{-3}$ in toluene solution) and high electroluminescent performances (EQE up to 17%).[12] Finally, the most recent molecular design to construct CP-TADF molecules has been described by the group of Chen. Their elegant approach relies on the so-called chiral-emitting-skeleton strategy where two fluorophores with no chirality and no TADF were linked together in order to produce axially chiral blue emitting CP-TADF molecule with high g_{lum} values of 4.5×10^{-3} in solution.[13] To summarize, so far, despite their more cost and time-effective synthetic pathways, CP-TADF molecules based on chiral perturbation are still lagging behind intrinsically chiral TADF molecules, notably in terms of dissymmetry factor values (g_{lum}). Surprisingly, a systematic investigation of key electronic and structural parameters (such as isomerism and symmetry of functionalization) in CP-TADF molecules remains unexplored. With the aim to overcome this limitation, we have designed novel chiral architectures and performed the first structure-properties relationship study of this family of molecules. In this paper, we describe novel molecular designs to construct CP-TADF molecules (Figure 2) based on chiral perturbation with the idea of shortening the distance between the active chromophore and the chiral perturbing unit to enhance the chiroptical properties. Ten pairs of chiral TADF molecules exhibiting aggregation-induced enhanced emission (AIEE) were synthesized in order to evaluate the impact of isomerism and carbazole substitution on the photophysical and chiroptical properties. This first structure-properties relationship study in CP-TADF materials notably resulted in g_{lum} values up to 3.0×10^{-3}, an unprecedented level for CPL molecules based on chiral perturbation strategy, providing valuable information for the development of such chiral emitters. Furthermore, we demonstrate for the first time the feasibility of top-emission CP-OLED assembly. Indeed, only bottom-emission CP-OLEDs built on glass substrates have been developed so far.[4] While these CP-OLED architectures obviously comply with the glass panel display manufacturing chain, their integration into future photonic devices may prove difficult, and even impossible for those involving

microtechnologies at silicon wafer level, such as optical communication or high resolution microdisplays. To address this issue, we present an innovative top-emission CP-OLED architecture suitable for wafer level processing and enabling CP light emission. As a proof of concept, a top-emission CP-OLED integrating novel CP-thermally activated delayed fluorescence (TADF) emitters has been designed and manufactured on the basis of current high resolution microdisplay silicon wafer level technology.

2. Results and Discussion

TADF molecules with CPL emission characteristics using the concept of chiral perturbation (Isomer **A**, Figure 1) have been developed in our group previously.[7] This powerful and flexible molecular design was then used by other groups to construct molecules exhibiting higher quantum yields or different emission colors with photoluminescence dissymmetry factors (g_{lum}) ranging from 0.5 to 1.2×10^{-3} (Figure 1).

Because the final application of these chiral emitters is related to their use as emissive dopants in CP-OLEDs, real-life benefits from these compounds can only be reached by a rational increase of their luminescence dissymmetry factors while maintaining equally high efficiency through TADF and AIEE phenomena. In this context, we have designed novel families of binaphthyl based TADF molecules which can be seen as structural isomers of the parent compounds derived from isomer **A** (see isomer **B**, **C′** and **C** Figure 2). In the first novel molecular design, the BINOL unit is placed at position 4,5 of a 1,2-phthalonitrile unit and the electron donors at position 3,6 (isomer **B**, an example of this molecular design is **B1**, Figure 2). Compared to the initial molecular design (isomer **A**, see Figure 1), shortening the distance between the chiral unit to the frontier orbitals of the active chromophore was expected to enhance the effect of chiral perturbation on the TADF D-A-D system (see HOMO-LUMO representation Figure 2).

Moreover, due to the steric congestion between the D-A-D system and the chiral unit, the D-A-D system may adopt a twisted conformation (see molecular design, Figure 2) which can enhance the chiroptical properties. Geometry optimization reveals that C-H-π intramolecular noncovalent interactions between hydrogens in position 3 and 3’ of the BINOL moiety and the carbazole aromatic rings restricts free rotations in this architecture leading to a global minimum (Figure S94, Supporting Information, page 94, IGM analysis.),[14] albeit not sufficiently well as to render the twisted D-A-D system configurationally stable (see also the crystal structures of **B1** Figure S102 (Supporting Information), page 102). In the second family of architectures, the chiral unit is placed at position 3,4 of the 1,2-phthalonitrile core, while acceptor and donor moieties are at position 5 for isomer **C′** (an example of this design is **C′1**) and 5,6 for isomer **C** (an example of this design is **C1**). DFT calculations show (Figure 2) that these isomers might possess a relatively low energy difference between the triplet and singlet excited states (ΔE_{ST}) due to the important spatial separation of their HOMO and LUMO orbitals (see Figure 2).

In the case of isomers **C′** (Figure 2, left) shortening the distance between the D-A active chromophore and the chiral unit compared to isomer **A** was expected to have a positive effect on the efficiency of the chiral perturbation from the BINOL unit onto the active

fluorophore. For isomer **C**, although the addition of a second carbazole unit may lead to an enhancement of the photophysical properties (increasing ε value and overall rigidity of the fluorophore), this may also imply a lower efficiency of the chiral perturbation due to spatial diffusion of the HOMO orbital coefficients on the two carbazole units. Based on these novel molecular designs, we have synthesized ten pairs of enantiomers involving differently substituted carbazoles in order to test experimentally our initial hypotheses, and to study the impact of the electron donor's nature on photophysical (QY, fluorescent decay, color emission) and chiroptical (g_{abs}, g_{lum}) properties.

2.1. Synthesis

To synthesize derivatives of isomer **B**, we started from commercially available tetrafluorophthalonitrile **1** and enantiopure BINOL (*R*)- or (*S*)-**2**. Using already described reaction conditions, intermediates (*R*)- and (*S*)- **3** and **4** were produced through a SNAr reaction at room temperature (see Scheme 1).[7] A selectivity of 100:13 in favor of isomer **3** for this step was determined by ^{19}F NMR (see Figure S103 in the Supporting Information).

This regioselectivity was found to increase when lowering the reaction temperature (100:8 at 0 °C, see Figure S104 in the Supporting Information). From intermediate **3**, different carbazole donors **5a-d** were introduced using K_2CO_3 as a base and DMF as the solvent. Compounds **B1–4** were thus obtained in a straightforward synthesis with isolated yields ranging from 20% to 87% depending on the nature of the carbazole moiety (see Supporting Information, page 6 for details). This difference in yields can be explained by the weak solubility of some carbazole derivatives (**5d** for instance), or separation issues due to coelution of impurities with the target compounds. However, all these syntheses can also be performed using a one-pot sequential approach, albeit with a slight drop in yields compared to the two-step sequences. Because the the SNAr reaction between **1** and **2** largely favors regioisomer **3**, another synthetic pathway was sought out in order to obtain isomers **C**. The selected strategy first involved the monofunctionalisation of **1** with carbazole **5a-c** (see Scheme 1,). A rapid screening of bases and solvents enabled us to obtain **6a-c** as major products (see Table S1 in the Supporting Information, page 15). However, we were not able to separate these products from small amounts of unreacted tetrafluorophthalonitrile **1**. Therefore, the crude product mixture was directly engaged in the second step, reacting it with enantiopure BINOL in DMF using K_2CO_3 as a base in order to obtain pure molecules **C′1–3** in reasonable yields after flash-chromatography purification (30–55% depending on the carbazole). Finally, the synthesis of derivatives of isomers **C** (**C1-C3**), involving a final step using classical conditions for such SNAr reactions between molecules **C′1-C′3** and carbazoles **5a-c**, was achieved in excellent yields.

2.2. Photophysics

The different molecules were studied in toluene solution and display obvious similarity in absorption spectra, in the high-energy UV region (300–340 nm accounting for π-π transitions located on the carbazole and the binaphtyl units). Although **A1**, **B1**, **C′1**, and **C1** feature the same components (BINOL, carbazole and phthalonitrile), significant differences due to isomerism arise on the low energy broad band spreading 340–450 nm (see Figure 3). This absorption region can be readily attributed to a charge transfer electronic transition

from carbazole(s) unit(s) to phtalonitrile in comparison to isomer **A1**. The latter displays a well-defined absorption band centered at 395 nm, **C′1** and **C1** show similar behavior (respectively located at 375 and 380 nm), whereas **B1** exhibits a structureless band around 345 nm. The wavelength shift of the charge transfer absorption band can be attributed to changes of the electrical transition dipolar moment between different isomers (see Table S5 in the Supporting Information, page 93).

TD-DFT calculations were used to simulate the absorption spectra and to determine the MOs involved in each transition (see Figures S74–S82 in the Supporting Information). The electronic spectra and the electronic transitions were analyzed using the Multiwfn 3.7 program.[15] The broad absorption band at the longest wavelength region in compounds **A1**, **B1**, and **C1** corresponds to the combination of different transitions. For **A1** and **C1** they originate mainly from HOMO → LUMO and HOMO-2 → LUMO excitations. For **B1** it arises from HOMO → LUMO and HOMO-1 → LUMO excitations. Finally, for **C′1**, the absorption band originates from HOMO → LUMO excitation (see Figure S89 in the Supporting Information). These absorption bands have a $\pi \rightarrow \pi^*$ nature and are caused by intramolecular charge transfer from electron donor to the phthalonitrile unit for $S_0 \rightarrow S_1$ (see Figure S93 in the Supporting Information) in all compounds and for $S_0 \rightarrow S_2$ in **A1** and **C1**. In **B1**, upon $S_0 \rightarrow S_2$ excitation a charge-transfer occurs from the electron donor to the phthalonitrile and BINOL units, while in **C′1**, the charge transfer occurs from the electron donor and BINOL units to the phthalonitrile unit. Compared to **A1** which possesses a maximum emission wavelength at ca 520 nm, **B1** possesses a significantly blue-shifted fluorescence emission with a $\lambda_{em\ max}$ at 470 nm whereas the color emission of the **C1** is situated in-between, with a maximum emission wavelength at ca. 490 nm. Because **C'1** possesses a lower number of donor unit compared to **C1**, the HOMO-LUMO gap tends to increase, and as a result, the emission of **C'1** is blue-shifted compared to the one of **C1** by around 10 nm ($\lambda_{em\ max}$ = 480 nm for **C′1**). In order to evaluate the impact of isomerism on the ΔE_{ST}, the energy level of S_1 and T_1 states were calculated using the def2-TZVP Functional with PBE0 Basis Set. Those calculations suggest that **B1, C′1**, and **C1** exhibit quite low ΔE_{ST} values of 54 meV for **B1**, 13 meV for **C′1**, and 136 meV for **C1**. In contrast, the ΔE_{ST} for **A1**, which was already experimentally demonstrated to be TADF active,[7] reaches the value of 171 meV.

The influence of the carbazole on the photophysical properties was then studied. As expected, the addition of *t*Bu and phenyl substituents in positions 3,6 of the carbazole units tends to increase the energy level of the HOMO resulting in a red shift of both absorption bands in the visible region and emission colors with $\lambda_{em\ max}$ at ca 470, 490, 505, and 515 nm for **B1**, **B2**, **B3**, and **B4** respectively (See Figure S4 in the Supporting Information). More interestingly, a dramatic impact of the substitution of the carbazole donor unit was observed on quantum yields of both prompt (Φ_{PF}) and delayed fluorescence (Φ_{DF}). Indeed, whereas the quantum yield of **B1** was found to be relatively low in toluene solution (with a value of Φ_{PF} around 2% measured in aerated solution), the presence of *t*Bu in positions 3,6 of the carbazole donors in **B2** gave significantly higher Φ_{PF} with a value of 11%. Substitution by phenyl groups had an even more beneficial effect on the QY with values of Φ_{PF} of 14% and 19% calculated for **B3** and **B4**, respectively. Fluorescence quantum yields

were also measured in the absence of triplet-quenching oxygen for a rapid evaluation of the potential TADF emission properties of molecules **B1**-**B4**. A non-significant increase of the QY was observed for **B1** in degassed solution. By contrast, Φ_{DF} ($\Phi_{DF} = \Phi_{Ar}–\Phi_{O2}$) of respectively 3%, 7% and 11% were determined for **B2**, **B3**, and **B4** respectively, when measuring their QY in the absence of oxygen. In order to investigate the emission properties of this series of compounds in solid state we prepared thin films by drop-casting toluene solutions of molecules **B1-B4** as a dopants (0.1% wt) in a poly(methyl methacrylate) matrix on quartz slides. Using an integration sphere to determine the absolute QY in thin films, Φ_F values of 7%, 16%, 18% and 30% were measured for **B1**, **B2**, **B3**, and **B4**, respectively. Finally, the TADF emission properties of all four compounds were confirmed by the observation of bi-exponential fluorescence decays. Generally, delayed fluorescence lifetime was found to be between 10 and 45 μs depending on carbazole substitution (see Table 1 for details and Figures S54–S63 in the Supporting Information for decays). In addition, TD-DFT calculations carried out for the optimized S_1 and T_1 state geometries reveal an important opposite rotation direction of the carbazole substituent group upon excitation for S_1 and T_1 states relative to the ground state S_0 (see Figure S92 in the Supporting Information).

Influence of the carbazole substitutions on the photophysical properties of series **C'** was also evaluated (See Figure S5 in the Supporting Information). As expected, introduction of *t*Bu and phenyl substituents led to a red shift of the visible region absorption bands (see Figure S2 in the Supporting Information) corresponding to the HOMO-LUMO transition. Such a red shift is also observed on the maximum emission wavelengths ($\lambda_{em\ max}$ = 480 nm for **C′1**, 504 nm for **C′2** and 510 nm for **C'3**, See Figure S5 in the Supporting Information). Molecule **C′1** has a Φ_{PF} of 14% and a Φ_{DF} of 6% with a QY reaching almost 20% in degassed toluene solution. Similar values were obtained for **C′2** and **C′3** with a highest value recorded for **C′3** with a QY of 22% in degassed toluene solution. Interestingly, the QY measured in thin films were found to significantly increase to 29%, 46% and 42% for **C′1**, **C′2**, and **C′3** respectively. These striking differences between QY values in solution and in thin films might be explained by restrained molecular motion in the polymer matrix. Compared to isomers **A**, **B** and **C** (where differences between QY in degassed toluene solutions and in thin films are much less pronounced), the donor unit in the **C′** series possesses a much higher degree of freedom due the lower steric congestion. Therefore, for isomers **C′**, the conformational disorder leading to nonradiative processes during relaxation of the excited state in solution might be limited in the thin film state. Finally, measurement of fluorescent decays has confirmed TADF emission of the molecules in this series, with τ_{DF} = 6, 19, and 17 μs for **C′1**, **C′2**, and **C′3**, respectively.

For Isomers **C** (See Figure S6 in the Supporting Information), as in the preceding series, a red shift of the emission bands is observed when *t*Bu and phenyl substituents are incorporated in positions 3,6 of the carbazole moiety. Interestingly, the measured values of Φ_{DF} were much higher in this series than for the **C'** series. Indeed, while Φ_{PF} exhibit very similar values of QY ranging from 13% to 20% when compared to isomers **C′**, Φ_{DF} tend to be higher in the **C** series, reaching values of 6%, 7% and 20% respectively for **C1**, **C2**, and

C3. In thin films, these relatively high quantum yields were confirmed, as well as the TADF emission, with τ_{DF} comprised between 18 and 40 μs.

Compounds derived from isomer **A** were shown to display aggregation induced emission enhancement properties.[8] In order to evaluate the potential AIEE properties of the novel **B**, **C′**, and **C** isomers, we have studied the fluorescence emission of each compound in solution as a function of the proportion of water (f_w) in THF. For every compound, in THF/water mixtures of up to $f_w = 0.5$, we observed a decrease of the emission compared to the initial conditions ($f_w = 0$). We then observed an upsurge of fluorescence for $f_w > 0.6$ (see Figures S36–S46 in the Supporting Information). In all cases, the novel isomers **B, C'** and **C** display AIEE properties, with a particularly pronounced increase of fluorescence intensity in the case of **C′1**, with an I/I_0 ratio of 5.6.

2.3. Chiroptical Properties

As mentioned in the introduction, one of our objectives in this study was to evaluate the influence of isomerism on the chiroptical properties of the title TADF emitters. At the ground state, the efficiency of the chiral perturbation provided by the BINOL unit can be evaluated looking at the dissymmetry factor g_{abs} values corresponding to the $S_0 \rightarrow S_1$ transition (see Figure 4). Comparison of these values for **A1**, **B1**, **C′1**, and **C1** highlights striking differences (see Figures S74, S75, S79, and S82 in the Supporting Information). For isomer **A**, a g_{abs} value of 0.53×10^{-3} was measured at the λ_{max} of the $S_0 \rightarrow S_1$ transition (situated around 430 nm). For **B1**, theoretical computations show that the charge-transfer band corresponds to an overlap of two transitions ($S_0 \rightarrow S_1$ and $S_0 \rightarrow S_2$) that can be experimentally observed thanks to the Cotton effect at 390 nm (See ECD spectra of **B1** Figure S22 in the Supporting Information). The g_{abs} value can be evaluated around 3×10^{-3} at 400 nm for $S_0 \rightarrow S_1$, whereas it only reaches 0.8×10^{-3} (370 nm) for $S_0 \rightarrow S_2$. The high value of g_{abs} for $S_0 \rightarrow S_1$ highlights the efficiency of the chiral perturbation at fundamental state for this molecule. In the case of isomer **C**, DFT calculations have shown that the HOMO possesses a higher orbital coefficient on the farthest carbazole from the BINOL.

This means that the barycenter of the active chromophore in **C1** is further away from the chiral unit than in **C′1**. For this reason, the dissymmetry factors for **C1** are much lower in the charge transfer area, ranging between 0 and 0.8×10^{-3} (depending on the transition observed), than the ones measured for **C′1**, which reach 1×10^{-3}.

In order to have a deeper understanding of the parameters governing the efficiency of the chiral perturbation, the magnitude of magnetic and electric transition dipole moments (respectively μ_m and μ_e) and their relative orientations for the $S_0 \rightarrow S_1$ and $S_0 \rightarrow S_2$ (see Tables S5 and S6 in the Supporting Information) transitions was determined computationally for all isomers. Indeed, theoretically, chiroptical properties are related to μ_m and μ_e, as well as θ, the angle between these vectors ($g = \frac{\mu_m}{\mu_e} \times 4\cos\theta$ Tables S5 and S6, Supporting Information).[16] This calculated value enables us to understand the influence and efficiency of the transition responsible in the first transition observed. Owing to the C_2 symmetry, a parallel orientation of μ_m and μ_e (z axis) is obtained for the $S_0 \rightarrow S_1$ transition (Figure 5) in **A1** and **B1** with a cancellation of components in the other directions (i.e., the x- and y

axis). For this reason, designs based on isomers **A** and **B** display an optimal orientation of transition dipole moments to maximize the chiral perturbation and therefore the chiroptical properties (with a value of $\theta = 0°$ for **A1** and $\theta = 180°$ for **B1**).

The higher value of g_{abs} for **B1** compared to **A1** accounts for a higher value of $|\mu_m|$ and a lower value of $|\mu_e|$ (see Table S5 in the Supporting Information). For **C'1** and **C1**, the relative orientation of the transition dipole moments are less favorable to maximize the g values ($\theta = 69°$ for **C1** and $\theta = 94°$ for **C′1**). However, for **C′1**, the magnitude of the electric and magnetic dipole transition moment vectors $|\mu_e|$ and $|\mu_m|$ are enhanced by factors of 2.9 and 3.8 respectively compared to **B1**. That is the reason why g_{abs} values corresponding to $S_0 \rightarrow S_1$ transition remain relatively high for C'1. Despite of the more favorable orientation of the electric and magnetic dipole transition moment vectors, the very low value of $|\mu_m|$ explain the experimental value of g_{abs} for **C1**.

In order to study the impact of isomerism on the chiroptical properties at the excited states, the g_{lum} values have been plotted as a function of wavelength (see Figure 6).

For **A1**, g_{lum} remains almost constant along the emission band centered at 520 nm with a value of 0.4×10^{-3}.[17] Surprisingly, for isomer **B1**, the g_{lum} value tends to decrease with the emission wavelength. Relatively high values of g_{lum} were measured with a maximum of 3.0×10^{-3} at the beginning of the emission band and a value of 2.0×10^{-3} at 472 nm ($\lambda_{em\ max}$). For isomer **C′1** the values of g_{lum} remain roughly constant along the emission band centered at 493 nm with a value of 1.0×10^{-3}. Isomers **C1** shows very low values of g_{lum} nearing zero at $\lambda_{em\ max}$ with an unusual bisignate pattern. The influence of the carbazole substituents on chiroptical properties was also studied. This influence was found to be extremely important in the isomer **B** series (see Figure 7 and simulated ECD spectra Figures S84–S87 in the Supporting Information).

While the addition of *t*Bu substituents did not drastically change the shape of either g_{abs} or g_{lum} as a function of the wavelengths, replacing them with phenyl groups led to a significant change in terms of chiroptical properties at the fundamental and excited states. Whereas for $S_0 \rightarrow S_2$ transitions g_{abs} values remain almost the same for all molecules in the **B** series, we can observe a disappearance of the Cotton effect on ECD spectra for **B3** and **B4**. This suggests that substitution of electron donor units by phenyl groups is detrimental to the efficiency of the chiral perturbation, as was confirmed by the lower value of $|\mu_m|$ calculated for $S_0 \rightarrow S_1$ transition of **B4** compared to **B1** (see Table S5 in the Supporting Information). This can also be seen in CPL measurements. In contrast to **B1** and **B2**, $g_{lum} = f(\lambda)$ curves of **B3** and **B4** adopt a sigmoidal shape (leading to a sign inversion of CPL along the emission band) and relatively lower intrinsic g_{lum} values between $+ 0.75 \times 10^{-3}$ and $- 0.5 \times 10^{-3}$ for (*R*)-**B3** and $+ 0.5 \times 10^{-3}$ and $- 0.5\ 10^{-3}$ for (*R*)-**B4**) are observed. Although g_{lum} values are relatively low, these two compounds exhibit a quite rare CPL sign modulation as a function of the emission wavelength. Because **B1** exhibits the highest value of g_{lum} in this series, we have synthesized an analogue **B1r** with an 5,5,6,6,7,7,8,8-octahydro-1,1-bi-2-naphthol moiety as chiral unit (see Figures S95–S97 in the Supporting Information). This structural modification did not lead to significant changes in both optical and chiroptical properties.[8b–c]

For the **C′** series the influence of the carbazole substituents on the chiroptical properties was found to be negligible (see Figures S26–S28 in the Supporting Information). Indeed, compounds **C′2** and **C′3** bearing *t*Bu or phenyl groups respectively in positions 3,6 show quite similar chiroptical properties to those of the parent molecule **C′1**, with g_{abs} values of around 0.8×10^{-3} at $\lambda_{abs\ max}$ for $S_0 \rightarrow S_1$ transition, and g_{lum} values of 1.0×10^{-3} at $\lambda_{em\ max}$. Indeed, theoretical investigations show that the nature of the substituent on the carbazole has little influence on the relative orientation and magnitudes of $|\mu_e|$ and $|\mu_m|$ (see Table S5 in the Supporting Information).

On the other hand, in the **C** series, the introduction of phenyl groups in position 3,6 of the carbazoles leads to an important enhancement of chiroptical properties as seen in molecule **C3** (see Figure 8).

Indeed, while the introduction of *t*Bu groups did not drastically change the values of chiroptical properties of **C2** versus **C1**, molecule **C3** exhibits much higher g_{abs} and g_{lum} values ($g_{abs} = 0.7 \times 10^{-3}$ at $\lambda_{abs\ max}$ $S_0 \rightarrow S_1$ transition and $g_{lum} = 0.7 \times 10^{-3}$ at $\lambda_{em\ max}$). This difference can be explained by a change in the orientation of the transition dipole moments. Indeed for **C3**, the angle θ between $|\mu_e|$ and $|\mu m|$ for $S_0 \rightarrow S_1$ transition was calculated to be 103°, much higher than that of **C1** (≈69°) and **C2** (≈49°) leading to a sign inversion observable on the ECD spectra in the $S_0 \rightarrow S_1$ transition region.

Optical and chiroptical properties of the ten new enantiomer pairs are reported in Table 1. Excitation of these compounds in the UV region covers the blue to green area in the visible spectrum, exhibiting TADF properties and quantum yields of up to 47% in the thin film state. Moreover, eight of them display relatively important signals in ECD on the $S_0 \rightarrow S_1$ transition, as well as circularly polarized luminescence. g_{lum} values range from 0.2×10^{-3} for compound **B3** to 3×10^{-3} for compound **B1**, the latter currently holding the highest value measured for chiral perturbation in a small organic compound.

These results demonstrate the important impact of both isomerism and carbazole substitution on the chiroptical properties of such chiral D-A chromophores. They highlight the high potential for these novel molecular designs based on isomers **B** and **C′** to imbue TADF molecules with valuable chiroptical properties.

2.3.1. Top-Emission CP-OLED Devices—So far, CP-OLEDs demonstrated by various research groups have exclusively focused on bottom-emission devices.[4] Despite very promising chiroptical characteristics as well as emission efficiencies, these devices are unfortunately unsuitable for current microelectronics technologies based on silicon wafer processing, which limits their application to large glass-panel displays. For instance, the bottom-emission CP-OLED technology does not allow the manufacturing of high-resolution displays that require depositing arrays of very small pixel pitch (typically less than 10 μm) onto a silicon-based CMOS driven integrated circuit used to control the emission of each individual OLED pixel for efficient video stream monitoring. As a result, only technologies based on the processing of top-emission OLEDs should be considered for these applications. In a top-emission OLED, the electroluminescent light is subjected to various multi-reflections inside the OLED stack (see Figure S98 in the Supporting Information)

making the control of emitted light polarization particularly challenging. That is why our purpose here is mainly assessing the feasibility of a top-emission CP-OLEDs through proofs of concept, rather than targeting maximum CP-OLED emission current efficiency and EQE. Because molecule **C′3** presents the best compromise between optical (Φ_F, ΔE_{ST}) and chiroptical properties (g_{lum} = 1.1 × 10^{-3}), it was used as the emitter to build the first top-emission CP-OLEDs. Several CP-OLEDs have thus been processed for this study. Details of the OLED processing procedure are provided in the Supplementary Information. The typical OLED stack integrating **C′3** chiral molecules is presented in Figure 9a. Figure 9c,d summarize the typical optoelectronic characteristics obtained with top-emission CP-OLEDs integrating either (*S*)-**C′3** or (*R*)-**C′3** chiral dopants. The emission spectra of these CP-OLEDs (induced by the chiral dopant) show green emission both centered at λ_{peak} = 510 nm (Figure 9). The corresponding *I–V–L* characteristics denote a clear rectifier diode behavior, low leakage current (≤1 μA cm^{-2}) and luminance performances of 6000 cd m^{-2} under 11V for the device involving the (*R*)-**C′3** chiral dopant. Overall, the OLED current efficiency can reach 2.5 cd A^{-1} with a corresponding external quantum efficiency EQE = 0.8% in the nominal luminance operating range of a display (500–1000 cd m^{-2}).

Chiroptical properties of these devices were measured in a second step using a CPL spectrometer. SiO/Al_2O_3-encapsulated single layers of pure chiral dopant (30 nm-thick, glass substrate) and corresponding CP-OLEDs were systematically compared. The most important result highlighted in Figure 10 is that the maximum dissymmetry factor |g| first measured on neat dopant single layers ($|g_{lum}|$ = 1.2 × 10^{-3}) is globally preserved after integration of the same dopant into a top-emission OLED ($|g_{El}|$ = 1.0 10^{-3}).[18] Chiroptical properties at the excited state were measured on the same apparatus for three different states (toluene solution, pure thin film and dopant in top emission OLED), and no significant difference in the g values (g_{lum} and g_{EL}) was observed.

This result clearly demonstrates for the first time the possibility of manufacturing top-emission CP-OLEDs able to preserve ~80% of the circular polarization induced by the chiral emitter dopant. Because of the particular optical behavior of top-emission OLED stacks, the emission spectra I(λ) and the dissymmetry factor spectra g(λ) of single layers of pure chiral dopant (**C′3**) and CP-OLED are different, and CP-OLED spectra appear systematically narrower. This behavior was expected since the OLED stack, with its two reflective electrodes, behaves as a selective optical band pass filter which reduces the OLED emission spectrum bandwidth. The central wavelength of such band pass filters depends on the thickness of the organic stack and, to a lower extent, on the thickness of the semi-transparent electrode. Ideally, the organic stack thickness must be thoroughly tuned so that the central wavelength perfectly matches the emission peak of the single EML layer. This optical tuning is very sensitive to any layer thickness error since a deviation of only 1 nm can induce up to a ≈5 nm spectral shift. In these first CP-OLED experiments, the optical cavity thickness was not fully optimized, hence the slight shift between the emission peaks of the single layer (λ_{peak} = 532 nm) and the CP-OLED (λ_{peak} = 510 nm). These first proofs of concept show that top-emitting CP-OLEDs could be indeed developed for high resolution microdisplay applications. However, they do not match so far the OLED specifications for microdisplays where at least 10 times higher current efficiency (≥20 cd

A^{-1}) and EQE (≥10%) are generally expected in the display nominal luminance operating range. Considerable room for improvement exists including i) the use of a host matrix providing much more efficient charge injection (mCP is rather resistive) and lower emission voltage threshold matching the capacities of CMOS driven integrated circuits (typically 2.5 V), ii) higher chiral dopant concentration for enhanced luminance, and iii) to a lower extent, a better alignment of the OLED optical cavity. Indeed, unlike bottom-emission OLEDs, the top-emission OLED architecture induces light spectral filtering (optical cavity effect) which reduces the light extraction efficiency. Calculations detailed in the supporting information (see Figure S99 in the Supporting Information) show that a better cavity alignment would have increased the emission intensity of our CP-OLEDs by around 15%.[19]

3. Conclusion

To summarize, we have described several innovative molecular designs of CP-TADF emitters using the chiral perturbation strategy. This first systematic study of the structure-(chiro) optical properties relationship focuses on the impact of isomerism of the electron donor relative to the chiral fragment, with the aim of identifying the key parameters that govern the absorption and luminescence dissymmetry factors (g_{abs} and g_{lum}) in these TADF and AIEE emitters. For each design, at least one carbazole unit is placed next to the binaphthyl unit to maximize the chiral perturbation efficiency. Among them, molecules derived from the **C′** series possess interesting $\mathbf{\Phi}_F$ (solid) including a TADF component, and good g_{lum} values, up to 1.1×10^{-3} in toluene solution, due to a high magnetic dipole moment, $|\mu_m|$ (for the $S_0 \rightarrow S_1$ transition). Increasing the electron density on the carbazole donor using *t*Bu, phenyl or *t*Bu-phenyl groups successfully enhances TADF efficiency without impacting the intensity of CPL. For the **C** series, adding one additional carbazole unit dramatically decreases the chiroptical properties due to an unfavorable orientation of the electric and magnetic dipole moments. Such an orientation can however modulate the electron density on both carbazole fragments (**C3**), resulting in higher values of dissymmetry factors of up to 0.62×10^{-3} for g_{abs} and 0.66×10^{-3} for g_{lum}. Finally, having both electron donors close to the chiral unit in the **B** series affords the best chiroptical properties for a chiral perturbation-based molecule, despite moderate quantum yields. Indeed, a g_{lum} value up to 3.0×10^{-3} was recorded for **B1**, due to a favorable orientation of the transition dipole moment, together with high values of $|\mu_m|$. However, modulating the electron density on carbazole fragments (**B3**, **B4**) is detrimental to CPL properties in this series, even though optical properties are still enhanced significantly.

Overall, this experimental and theoretical study shows that the interplay between TADF and CPL properties is far from trivial and proves difficult to anticipate. Our investigation notably highlights the importance of maximizing the value of $|\mu_m|$ and the resulting angle between the electric and magnetic dipole moments, θ, to find the best compromise between TADF and CPL efficiencies. In terms of applications, we have achieved the first proof of concept of circularly polarized top-emission OLEDs. The proposed device architecture as well as its manufacturing technology were shown to preserve 80% of the initial circular polarization of chiral emitters. Moreover, these devices meet the requirements of silicon-based high-resolution microdisplay technology, paving the way to other microelectronics-related photonics applications. Ongoing work is dedicated to performance improvements of top-

emission CP-OLEDs, notably in order to optimize the stack and find new solutions to limit the reflection of light inside these devices to improve the degree of electroluminescence polarization.

Supplementary Material

Refer to Web version on PubMed Central for supplementary material.

Acknowledgements

G.P. thanks the SCBM, the Labex CHARMMMAT (ANR-11-LABX-0039), the “Programme Transverse de Competences du CEA” (POLEM project), and the ANR (iChiralight project, ANR-19-CE07-0040) for funding and support. David Buisson, Elodie Marcon, Céline Chollet, Amélie Goudet, and Sabrina Lebrequier are also warmly acknowledged for their contribution in this work (HPLC analysis and purification). G.M. thanks the NIH, Minority Biomedical Research Support (Grant No. 1SC3GM089589-08), and the Henry Dreyfus Teacher-Scholar Award for financial support. G.C. and G.P. thanks Arnaud Brosseau for his precious help for fluorescent decay measurements.

References

[1]. Wong MY, Zysman-Colman E, Adv. Mater2017, 29, 1605444.

[2]. Im Y, Kim M, Cho YJ, Seo J-A, Yook KS, Lee JY, Chem. Mater2017, 29, 1946.

[3]. Uoyama H, Goushi K, Shizu K, Nomura H, Adachi C, Nature2012, 492, 234. [PubMed: 23235877]

[4]. Zhang D-W, Li M, Chen C-F, Chem. Soc. Rev2020, 49, 1331. [PubMed: 31999286]

[5]. Pieters G, Frederic L, in Circularly Polarized Luminescence of Isolated Small Organic Molecules, (Ed: Mori T), SpringerSingapore, Singapore2020, Ch. 13.

[6]. Imagawa T, Hirata S, Totani K, Watanabe T, Vacha M, Chem. Commun2015, 51, 13268.

[7]. Feuillastre S, Pauton M, Gao L, Desmarchelier A, Riives AJ, Prim D, Tondelier D, Geffroy B, Muller G, Clavier G, Pieters G. g., J. Am. Chem. Soc2016, 138, 3990. [PubMed: 26967372]

[8]. a)Song F, Xu Z, Zhang Q, Zhao Z, Zhang H, Zhao W, Qiu Z, Qi C, Zhang H, Sung HHY, Williams ID, Lam JWY, Zhao Z, Qin A, Ma D, Tang BZ, Adv. Funct. Mater2018, 28, 1800051;b)Wu Z-G, Han H-B, Yan Z-P, Luo X-F, Wang Y, Zheng Y-X, Zuo J-L, Pan Y, Adv. Mater2019, 31, 1900524;c)Sun S, Wang J, Chen L, Chen R, Jin J, Chen C, Chen S, Xie G, Zheng C, Huang W, J. Mater. Chem. C2019, 7, 14511;d)Wu Z-G, Yan Z-P, Luo X-F, Yuan L, Liang W-Q, Wang Y, Zheng Y-X, Zuo J-L, Pan Y, J. Mater. Chem. C2019, 7, 7045.

[9]. Wang Y, Zhang Y, Hu W, Quan Y, Li Y, Cheng Y, ACS Appl. Mater. Interfaces2019, 11, 26165. [PubMed: 31240905]

[10]. a)Li M, Li S-H, Zhang D, Cai M, Duan L, Fung M-K, Chen C-F, Angew. Chem., Int. Ed2018, 57, 2889;b)Wang Y-F, Lu H-Y, Chen C, Li M, Chen C-F, Org. Electron2019, 70, 71.

[11]. Zhang M-Y, Li Z-Y, Lu B, Wang Y, Ma Y-D, Zhao C-H, Org. Lett2018, 20, 6868. [PubMed: 30359038]

[12]. Sharma N, Spuling E, Mattern CM, Li W, Fuhr O, Tsuchiya Y, Adachi C, BrÃ¤se S, Samuel IDW, Zysman-Colman E, Chem. Sci2019, 10, 6689. [PubMed: 31367323]

[13]. Li M, Wang Y-F, Zhang D, Duan L, Chen C-F, Angew. Chem., Int. Ed2020, 59, 3500.

[14]. Lefebvre C, Rubez G, Khartabil H, Boisson J-C, Contreras-García J, Hénon E, Phys. Chem. Chem. Phys2017, 19, 17928. [PubMed: 28664951]

[15]. Lu T, Chen F, J. Comput. Chem2012, 33, 580. [PubMed: 22162017]

[16]. a)Tanaka H, Ikenosako M, Kato Y, Fujiki M, Inoue Y, Mori T, Commun. Chem2018, 1, 38;b)Sánchez-Carnerero EM, Agarrabeitia AR, Moreno F, Maroto BL, Muller G, Ortiz MJ, de la Moya S, Chem. - Eur. J2015, 21, 13488. [PubMed: 26136234]

[17]. As reported in reference 7, g_{lum} values of +/− 1.2×10^{-3} were determined for **A1** using a homemade CPL spectrophotometer. Using a commercially available CPL spectrophotometer, g_{lum} values around +/− 0.4×10^{-3} were measured (see Figure 6).

[18]. By contrast with the results described in reference 8a, but in accordance, with results reported in references 8b and 8c, for molecule **A1, B1**, and **C′3** no appreciable chiroptical properties amplification was found in thin film (measuring CPL responses of pure thin films fabricated by spin coating or thermal evaporating method). In our hands, g_{lum} values of compounds *R*/*S*-BN-DCB described in reference 8a in diluted toluene solution ($C = 10^{-5}$) and in pure thin film (fabricated using thermal evaporating method) were found to be $<10^{-3}$ (measured with two different CPL spectrometers using different samples).

[19]. Note that for this proof-of-concept top emission CP-OLED, we have chosen to use Ca as the electron injection layer in order to limit light reflection, and therefore maximize the chance to conserve the circularly polarized electroluminescence generated by the EML. This may also significantly contribute to decrease the efficiency of the device (in terms of EQE).a)Zinna F, Giovanella U, Bari LD, Adv. Mater2015, 27, 1791; [PubMed: 25604886] b)Zinna F, Pasini M, Galeotti F, Botta C, Di Bari L, Giovanella U, Adv. Funct. Mater2017, 27, 1603719.

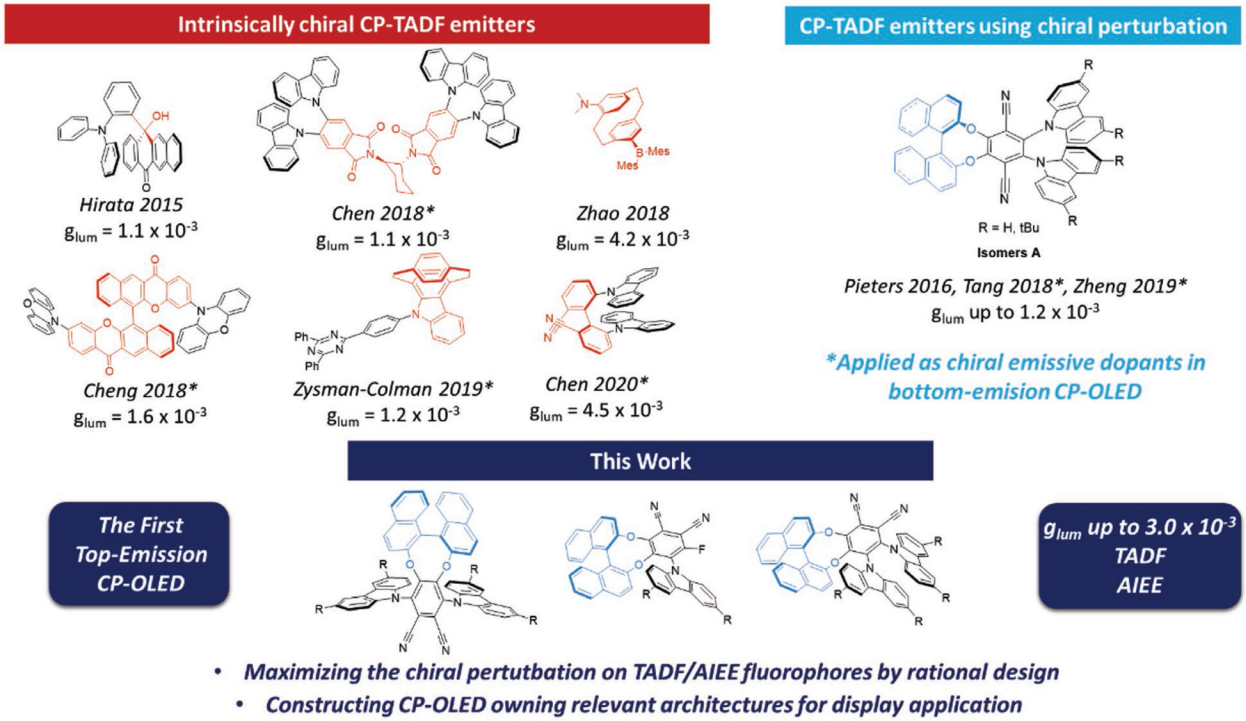

Figure 1.

Molecular designs reported so far to construct CP-TADF molecules (g_{lum} values reported in toluene solution) and new molecular designs explored in this work.

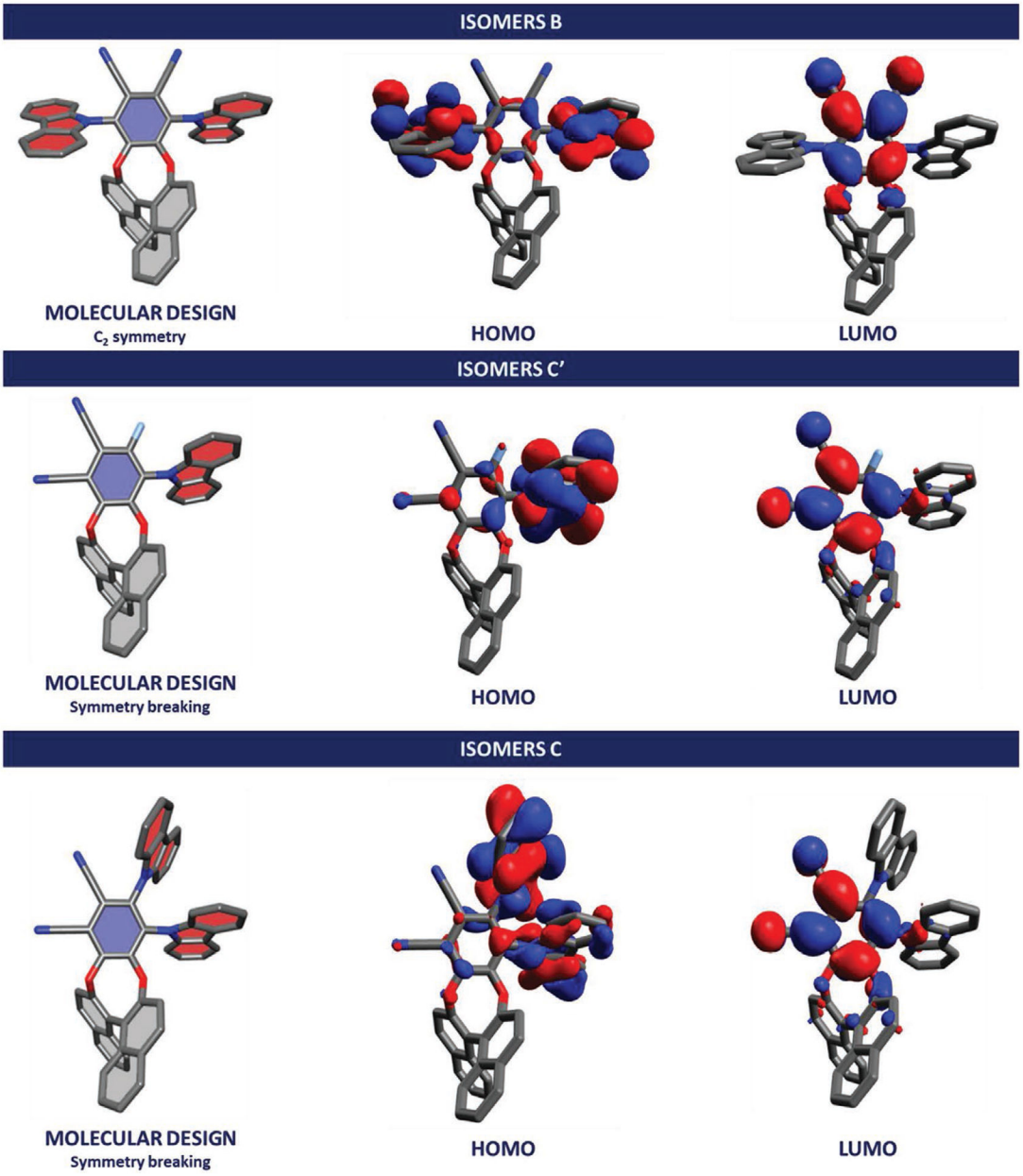

Figure 2.
Isomers of CP-TADF molecules investigated in this study.

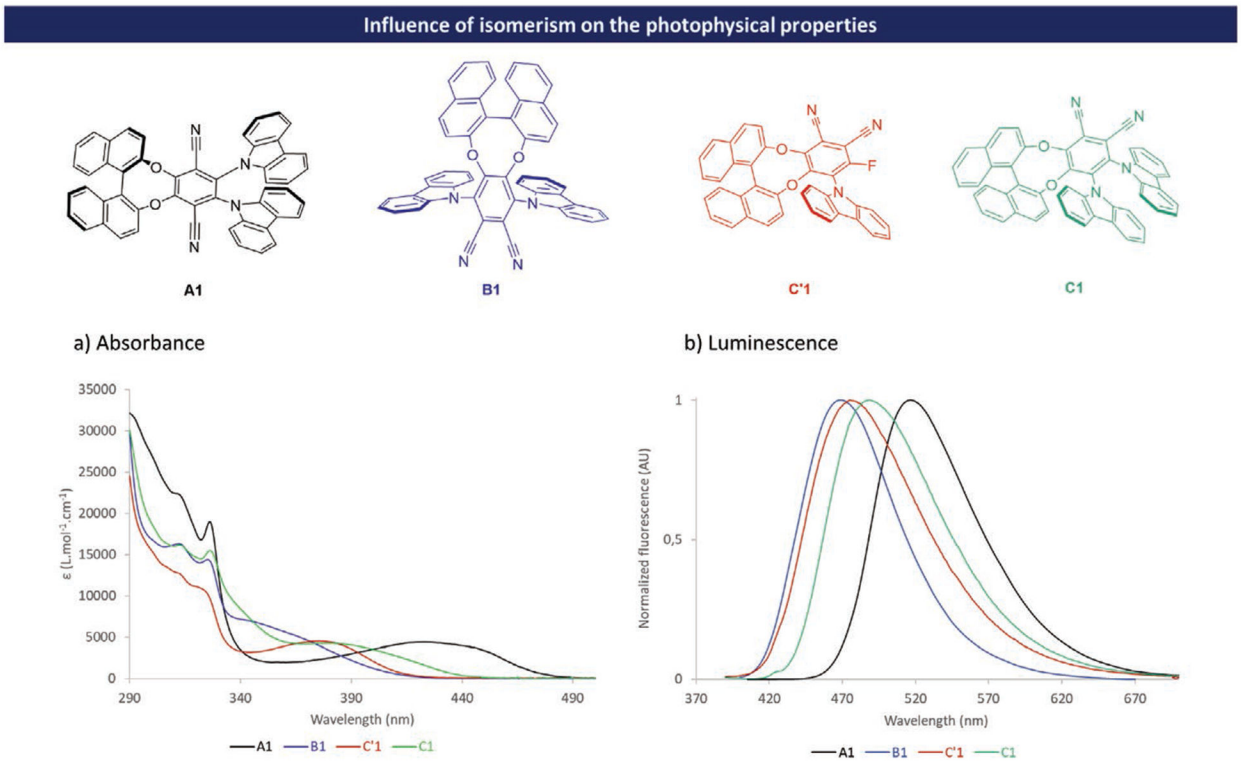

Figure 3.

Influence of isomerism on the photophysical properties: a) absorption ($C = 1 \times 10^{-3}$ M in toluene); b) luminescence ($C = 10 \times 10^{-6}$ M in toluene); **A1** in black, **B1** in blue, **C′1** in red, and **C1** in green.

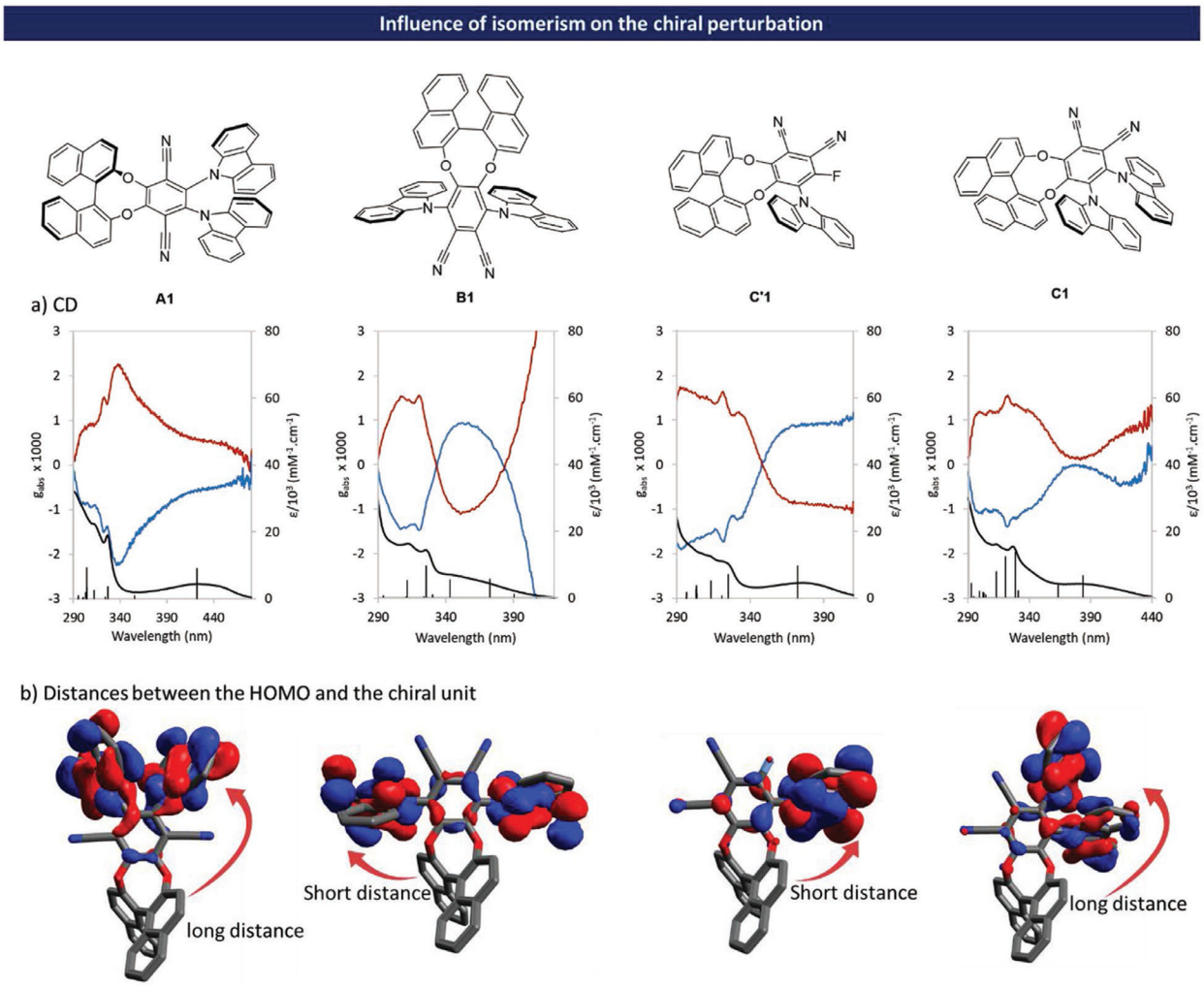

Figure 4.

Influence of isomerism on chiroptical properties: a) UV (in black) and g_{abs} (color) spectra measured in toluene at 1×10^{-3} M, oscillator strengths are plotted to visualize transitions but are not scaled. For $g_{abs} = f(\lambda)$ blue traces correspond to molecules with (*R*)- configuration and red traces correspond to molecules with (*S*)-configuration; b) HOMO of the four different isomers.

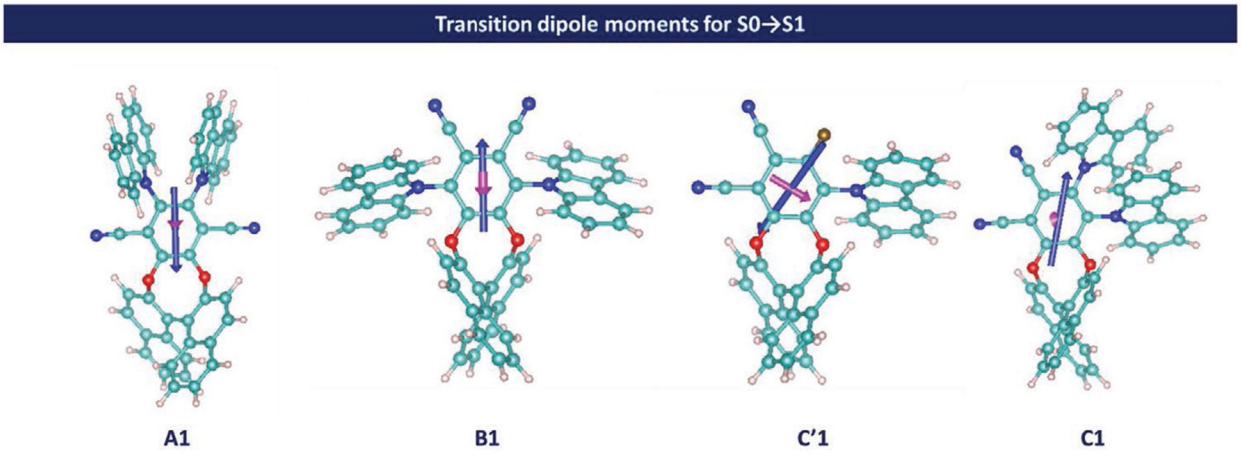

Figure 5.
Schematic representation of electric (blue) and magnetic (magenta) transition dipole moments of the $S_0 \rightarrow S_1$ transition.

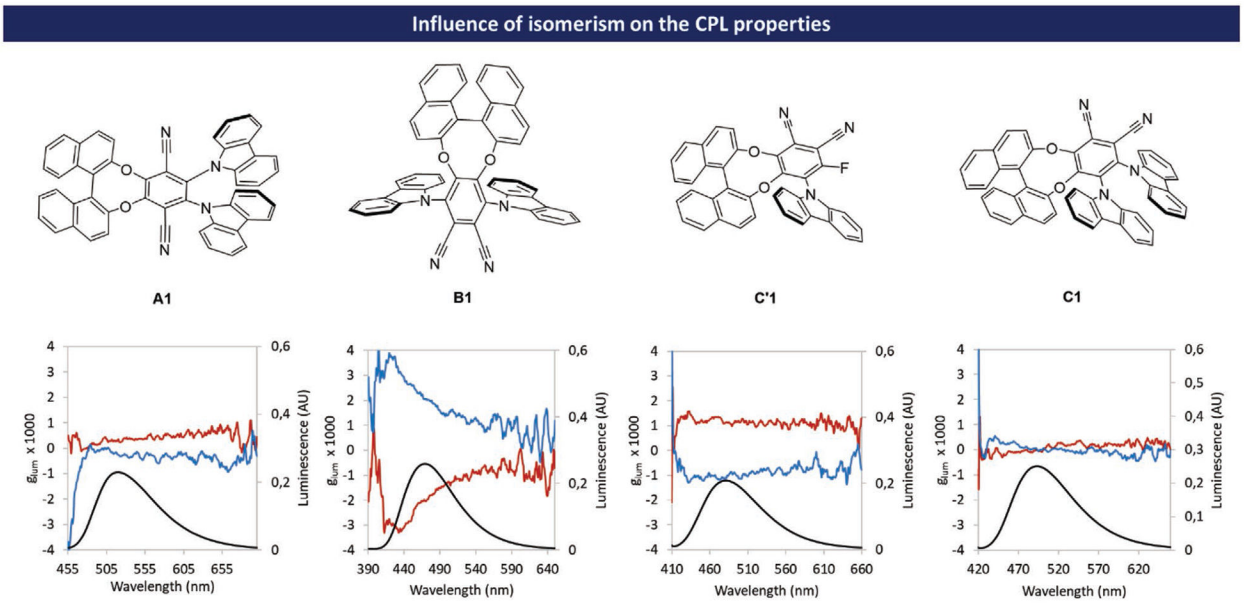

Figure 6.

Influence of isomerism on the chiroptical properties at the excited state. $g_{lum} = f(\lambda)$ in toluene solution, blue traces correspond to molecules with (*R*)- configuration and red traces correspond to molecules with (*S*)-configuration; black traces correspond to fluorescence spectra.

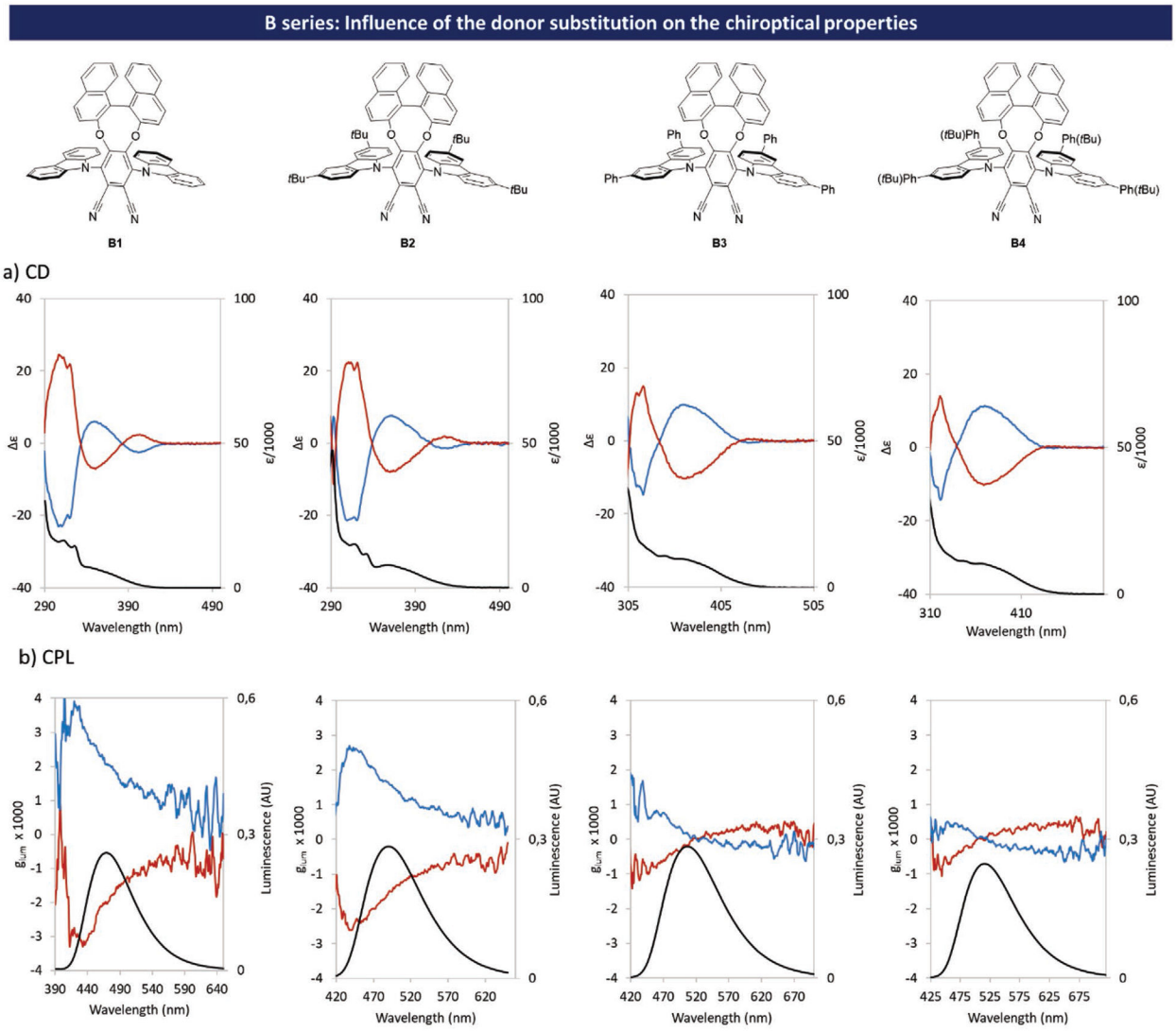

Figure 7.

Influence of carbazole substitution on chiroptical properties in the isomer **B** series: a) absorbance (black trace) and CD (measured at $C = 1 \times 10^{-3}$ M in toluene); b) CPL and fluorescence (fluorescence spectra measured at optical density near 0.2 in toluene); blue traces correspond to molecules with (*R*)-configuration and red traces correspond to molecules with (*S*)-configuration.

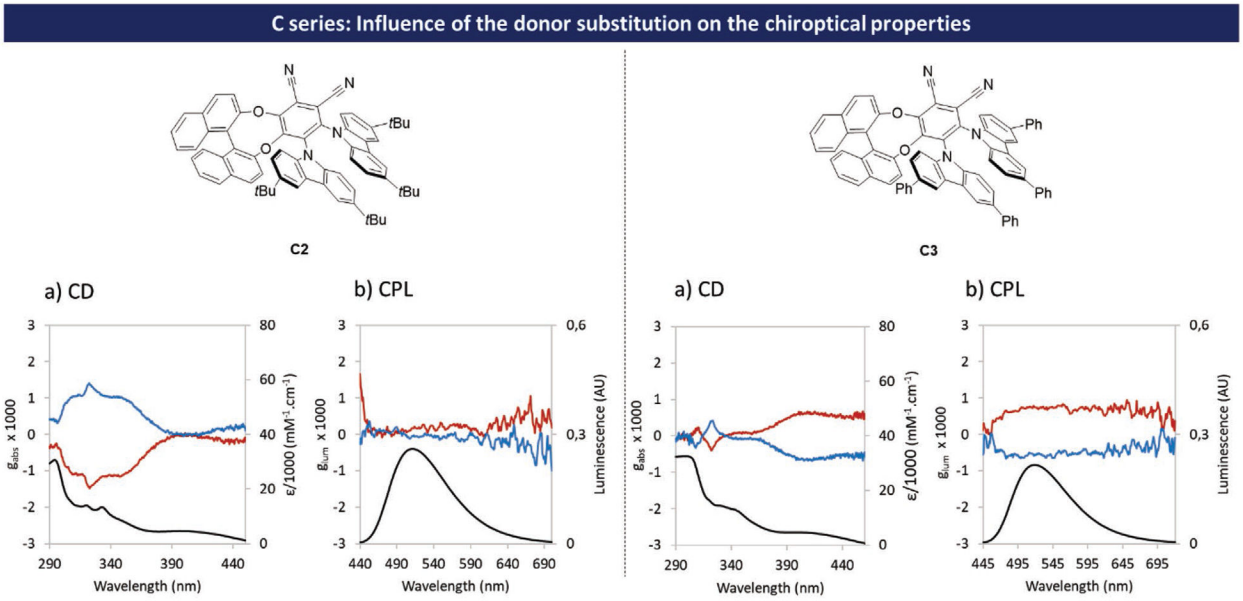

Figure 8.

Influence of carbazole substitution in the isomer **C** series on chiroptical properties in toluene solutions (fluorescence and CPL spectra measured at optical density near 0.2; UV and CD spectra measured at 1×10^{-3} M; black traces correspond to absorbance or fluorescence (for CD and CPL respectively), red traces correspond to molecules with (*S*)-configuration and blue traces correspond to molecules with (*R*)-configuration.

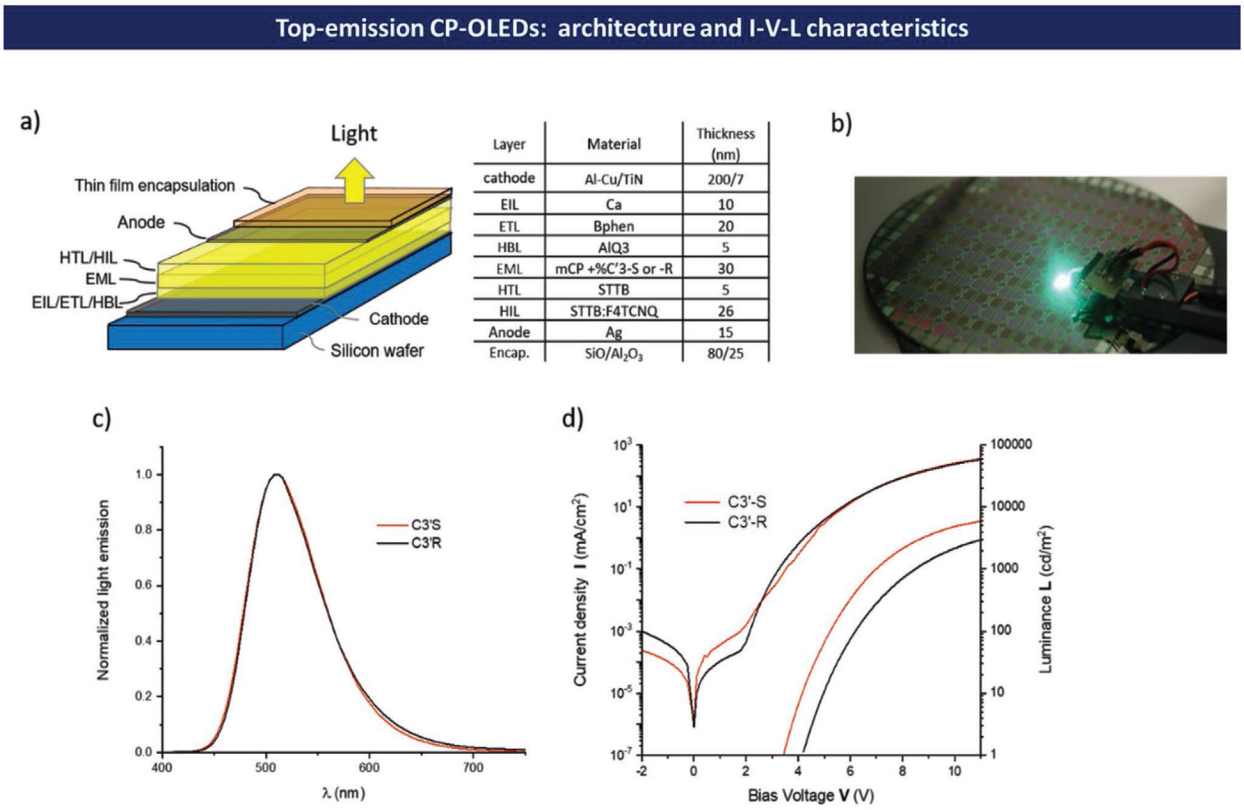

Figure 9.

a) Typical thin film stack used to build a top-emission CP-OLEDs with the (*R*)-**C′3** and (*S*)-**C′3**-S chiral dopants synthesized in this work; b) 8-inch wafer level-processed CP-OLEDs showing an individual CP-OLED under test; c) Light emission spectrum of CP-OLEDs integrating either (*S*)-**C′3** or (*R*)-**C′3** chiral dopants; d) Corresponding *I*–*V*–*L* characteristics.

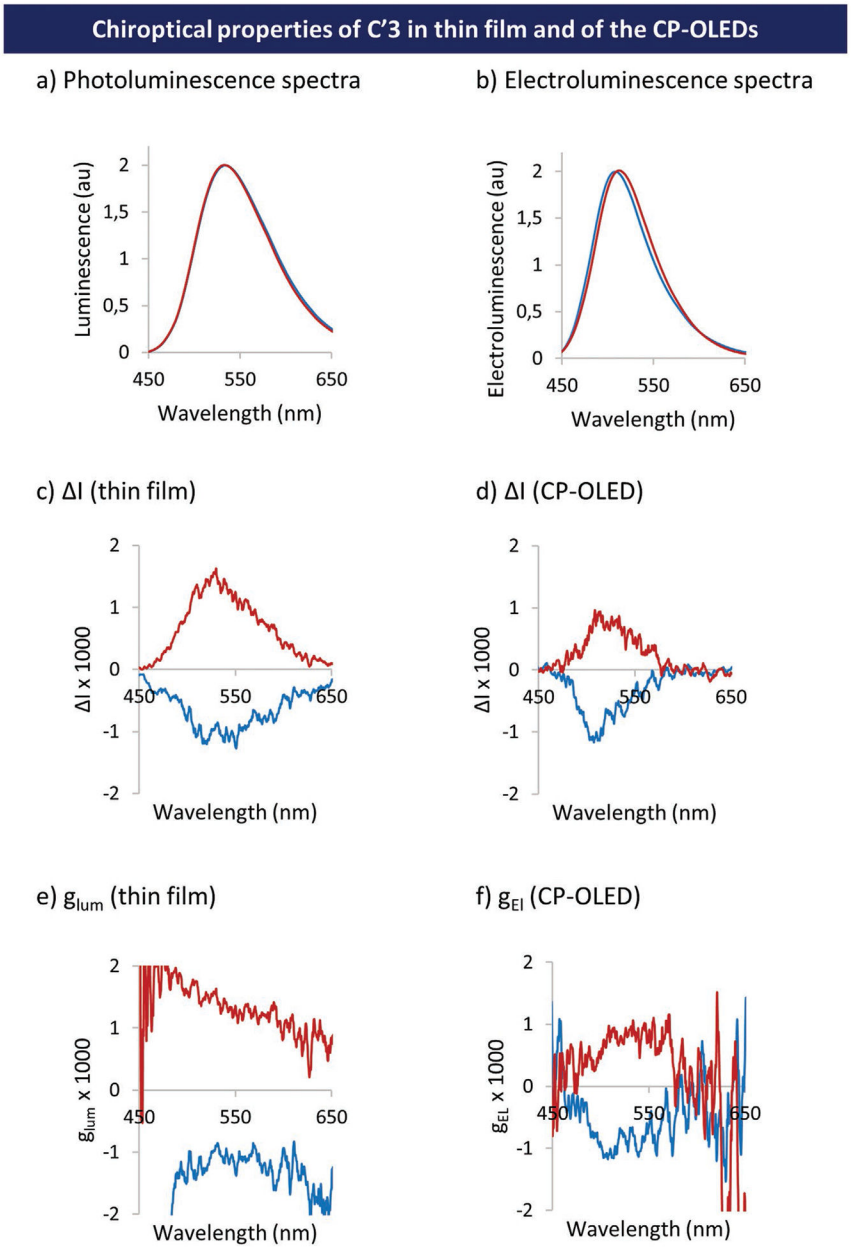

Figure 10.

a) Photoluminescence response of single layers of pure **C′3**; b) electroluminescence response of the top-emission CP-OLEDs; c) $\Delta I = f(\lambda)$ curves related to single layers of pure **C′3**; d) $\Delta I = f(\lambda)$ curves related to the electroluminescence generated by the CP-OLEDs; e) $g_{lum} = f(\lambda)$ curves obtained for single layers of pure **C′3**; f) $g_{El} = f(\lambda)$ curves related to the electroluminescence generated by the top-emission CP-OLEDs; red traces correspond to molecules with (*S*)-configuration and blue traces correspond to molecules with (*R*)-configuration.

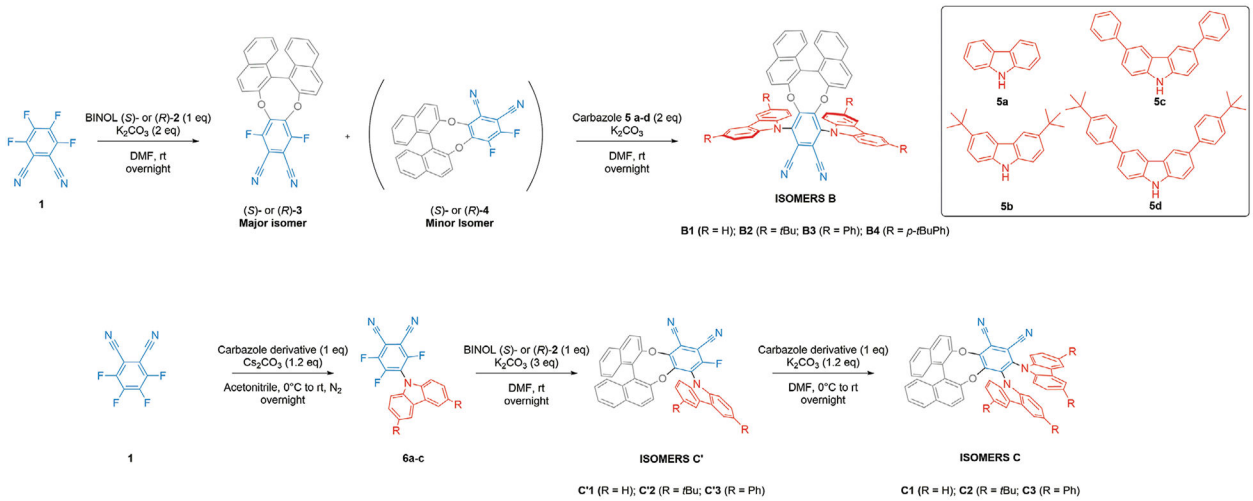

Scheme 1.

Synthesis of isomers **B**, **C′** and **C**.

Table 1.

Summary of optical and chiroptical properties for the **B**, **C′**, and **C** isomer series.

Compound	$\lambda_{abs\ S0\rightarrow S1}$ [nm]	$\lambda_{em\ max}$ [nm]	Φ_F (solid)	τ_{PF} [ns]; τ_{DF} [μs]	ΔE_{ST} [a)] [meV]	$g_{abs} \times 10^3$ (at $\lambda_{abs\ max}$)	$g_{lum} \times 10^3$ (at $\lambda_{em\ max}$)
B1	345	469	7	8; 10	310 (54)	1.1	2.1
B2	358	490	16	23; 45	180 (51)	1.0	1.6
B3	364	506	18	22; 39	160 (17)	1.0	0.2
B4	370	516	30	43; 16	100 (22)	1.0	<0.1
C'1	375	481	29	10; 6	280 (13)	0.9	1.1
C'2	393	504	46	12; 19	130 (53)	0.8	1.0
C'3	395	510	42	11; 17	110 (9)	0.9	1.1
C1	380	493	25	11; 18	220 (136)	<0.1	<0.1
C2	396	511	31	11; 40	110 (70)	<0.1	<0.1
C3	400	519	47	15; 22	100 (75)	0.7	0.7

[a)] Estimated experimental ΔE_{ST} measured in 2-methyltetrahydrofurane at 77 K (see Figures S17–20 and Table S2, Supporting Information) and theoretical values calculated using the def2-TZVP Functional with PBE0 Basis Set (in brackets).